J. Fluid Mech. (1977), *vol.* 79, *part* 3, *pp.* 463–480
Printed in Great Britain

Directional slope and curvature distributions of wind waves

By JIN WU

College of Marine Studies, University of Delaware, Newark

(Received 23 January 1976)

The slope and curvature distributions of wind waves along two principal axes (upwind–downwind and cross-wind) have been measured in a laboratory tank under various wind velocities. In both directions, the slope distributions are very closely Gaussian, and the components of the mean-square water-surface slope vary logarithmically with the friction velocity of the wind. As the wind velocity increases, the ratio of the upwind–downwind and cross-wind components increases and lies between 0·5 and 0·6 at high wind velocities in the gravity-governed regime of wind–wave interaction. The radius of water-surface curvature, along either direction of measurement, is generally found to be greater at a steeper viewing angle from the normal to the mean water surface. The average radius of curvature of the disturbed surface varies inversely with the friction velocity of the wind. The ratio of the upwind–downwind and cross-wind components of the average radius of curvature is unity at all wind velocities, indicating that the wind-disturbed water surface is isotropic on the smallest scale. Other results show that both the slope and the curvature distributions are asymmetric along the upwind–downwind direction, either because of the presence of parasitic capillaries or because of the occurrence of wave breaking. The results also indicate that even the high frequency portion of the spectrum is saturated locally but the spectrum is not universal, and that the long waves suppress the growth of the nearly saturated ripples.

1. Introduction

The sea surface features ripples riding on long waves. There has been a great deal of interest in describing statistically the microstructure of the wind-disturbed surface, i.e. the pattern of ripples. These wavelets are involved in the inception of wind waves as well as in the dissipation of wave energy (Phillips 1966). The microstructure also governs the reflexion and back-scattering of electromagnetic waves (Newton & Rouse 1972) impinging on the air–sea interface and the radiation of thermal energy (McGrath & Osborne 1973) from it.

Previous laboratory measurements (Schooley 1954; Cox 1958; Wu 1971*a*) have determined the upwind–downwind components of the mean-square slopes of the disturbed water surface under various wind velocities. It has been considered that the narrowness of the tank limits the growth of cross-wind components; these components, however, have not been measured in the laboratory.

Distributions of upwind–downwind curvature of the disturbed water surface have also been measured (Wu 1972*a*), but there have been no measurements of cross-wind curvatures either.

In the present study, the distributions of upwind–downwind and cross-wind slope and curvature of the disturbed surface were systematically measured under various wind velocities. The results, containing the first systematic description of the microscopic structure of wind waves, are important for studying and modelling the air–sea interface. In addition, comparisons between the components measured along two principal axes and between field and laboratory results may provide some insight into energy-transfer processes from wind to waves and among wave components.

2. Wind and wave conditions

The experiments were conducted in a wind-wave tank 1·5 m wide and 22 m long. Mounted at the upwind end of the tank is an axial-flow fan, driven by a variable-speed motor; a permeable wave absorber is installed at the downwind end. The tank is covered for the first 15 m to provide an 0·31 m high wind tunnel above 1·24 m deep water. The test section is located at the middle of the tank length.

The wind boundary layer over the water surface has been surveyed with a Pitot–static probe. As reported earlier (Wu 1968, 1975), the wind-velocity profiles in the tunnel follow the logarithmic law near, but not very close to, the water surface. On the basis of the friction velocity and roughness length, determined from the wind profile, it was deduced that the wind boundary layer in the present tank became turbulent for $U > 2{\cdot}0$ m/s and became aerodynamically rough for $U > 2{\cdot}5$ m/s. Rhombic gravity wave cells were formed as soon as the wind boundary layer became turbulent. As the wind velocity increased beyond 3 m/s, parasitic capillaries were produced; this is the surface-tension-governed regime of wind–wave interaction. Wave breaking was observed at high wind velocities $U > 7$ m/s, where gravity replaces surface tension as the governing parameter of wind–wave interaction.

From the wave profile measured with a conductivity probe, periods of more than 100 basic waves were obtained for each wind velocity. The average wavelength was then calculated from the average period with the influence of wind-induced drift currents taken into account. The average lengths and heights of dominant waves along with the friction velocity of the wind have been presented elsewhere (Wu 1975).

3. Measurements of microstructure

Optical instrument

The optical instrument, shown in figure 1 (*a*) (plate 1), is supported on a carriage between two vertical circular-arc plates with their geometric centres at the mean water surface. The light sheet produced by the light source and the axis of the telescope lie in the same radial plane. The lenses of the light box and of the tele-

scope are focused on the mean water surface at the midspan of the vertical plates, which is on the centre-line of the tank. By means of sprockets and an endless chain, the carriage can be placed anywhere along the arc so that the viewing angle of the optical instrument may be set at any desired inclination to the mean water surface. With such arrangements, the photomultiplier receives reflected light only when the water surface is normal to the radial plane containing the light sheet and the telescope's axis. The cross-section of the light sheet is rectangular, with a large length-to-width ratio (20:1) and with its short side aligned with the direction of measurement, the observation plane within which the instrument traverses. The calibrated slope response of the instrument to the water-surface slope in the direction of interest is seen in figure 1(*b*) to have an angular tolerance slightly greater than 1°; the tolerance in the transverse direction is, therefore, about 20°.

As shown in figure 1(*a*), the two vertical plates, joined together by a base plate, are supported on top of a base ring. The base plate can be rotated to align the observation plane at any desired angle with respect to the wind direction. Measurements have been conducted in the present experiment along two principal directions: upwind–downwind and cross-wind.

The focal spot of the telescope on the water surface, 0·7 mm in diameter, is completely bright when the water surface is relatively flat and partially bright when the curved water surface reflects part of the impinging light away from the telescope (see figure 1 *c*). It may be worthwhile to note that the viewing area of the telescope is sufficiently small that the chances of the instrument sensing two capillary waves simultaneously are almost nil. The width ($2h$) of the bright portion of the spot is related to the surface curvature, and the signal intensity is proportional to the ratio of the bright area to the total area of the spot. The calculated and calibrated curvature response of the instrument are shown in figure 1 (*c*). If a small focal spot is adopted for the telescope and the instrument is placed far enough from the water surface, the instrument has the same response for concave and convex surfaces having curvature of the same magnitude.

The light signal is continuous and saturated to a prescribed level, i.e. insensitive to a change in surface curvature as long as the change in the angle of the wavy water surface from one face to the other is less than the acceptance width of the instrument (about 1°). As the angular change increases further, the signal becomes a light pulse. The intensity of the signal, the pulse height, is related to the surface curvature; the period of the signal, the pulse width, is the time required for a detectable water-surface slope to pass the instrument. The details of this instrument have been reported elsewhere (Wu 1972*a*).

Experimental procedure and data acquisition

Two series of experiments have been conducted in the present study to measure the microstructure of the disturbed surface under various wind velocities along both the upwind–downwind and the cross-wind direction. For each wind velocity, the optical instrument was set successively at various angles of inclination from the mean water surface, the data being taken over a constant period of 4 min for each inclination. The signal produced by the reflecting water surface was fed

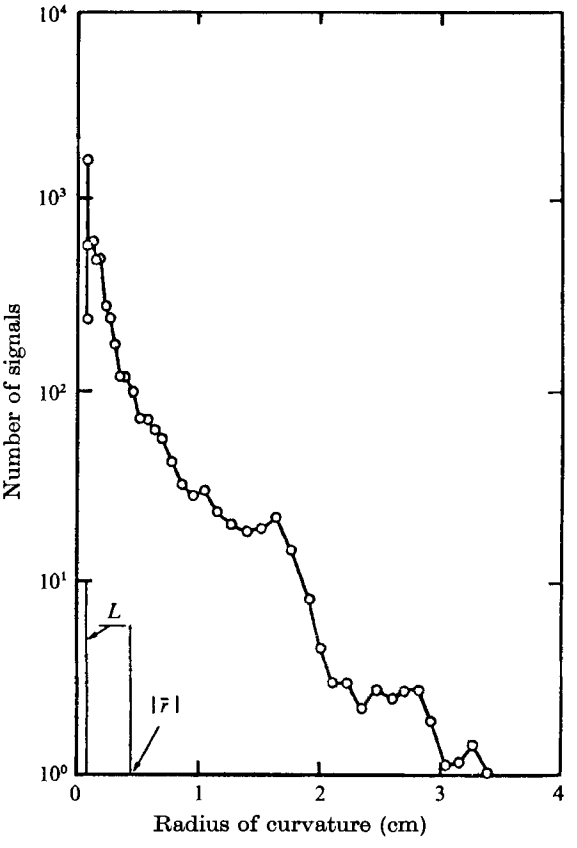

FIGURE 2. Typical data. L indicates the lower cut-off of the instrument and $|\bar{r}|$ is the average radius of curvature.

continuously into a pulse-height analyser and sorted automatically according to its intensity into one of the channels of the analyser; each channel has a preset intensity band. From the analyser, the intensity distribution of light pulses which accumulated during a constant period of time for a given instrument inclination was obtained and subsequently digitized. It is noted that the period of the pulse was compared first with a preset time interval of 0·001 s, the ratio of the pulse period to this preset time interval being calculated. A pulse with period shorter than the preset interval was counted as one and a pulse with period longer than a certain multiple of the preset interval was counted as the next integer.

A sample set of data on the pulse-height distribution is shown in figure 2, where the horizontal axis has been transformed from the channel number (or voltage) into the radius of curvature. The lower cut-off radius of curvature L of the present optical instrument is marked by one long vertical line on the left of figure 2. Set well above the instrument noise, this lower cut-off is about 1·7 % of the maximum detectable radius of curvature. The upper cut-off (i.e. the maximum detectable) radius of curvature is selected at 4 cm. A wavy surface with a radius of curvature beyond the upper cut-off would be registered as the value of the upper cut-off.

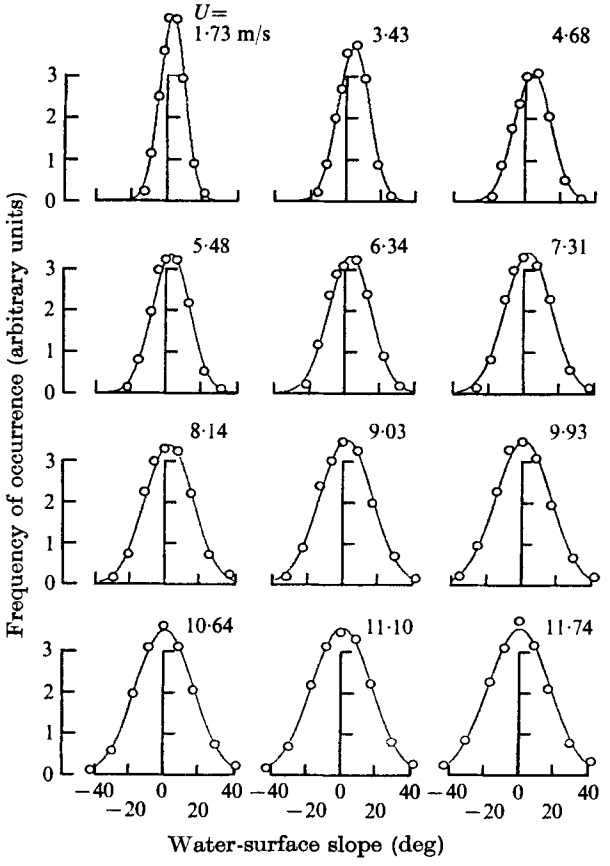

FIGURE 3. Distributions of upwind–downwind slope under various wind velocities.

However, except at very low wind velocity, less than 2 m/s, the radius of curvature of the water surface seldom reaches the upper cut-off. The centroid of the area (shown in figure 2) enclosed by the measured distribution curve, the horizontal axis and the lower cut-off radius of curvature is then determined. This calculated centroid, indicated as $\bar{r}$ in the figure, is the average absolute radius of curvature, since the present optical instrument, as discussed earlier, does not discriminate between concave and convex surfaces.

4. Results

Slope distributions and root-mean-square slopes

As discussed in the previous section, for each wind velocity the optical instrument was set successively at various angles of inclination, and the signals were automatically sorted. From the data, a sample of which is shown in figure 2, the total number of signals for one angle of observation can be obtained. Compiling the total number of signals for various angles which accumulated over a constant period of time, we have the relative frequency of occurrence, or the distribution of the water-surface slope. Distributions of upwind–downwind slope under

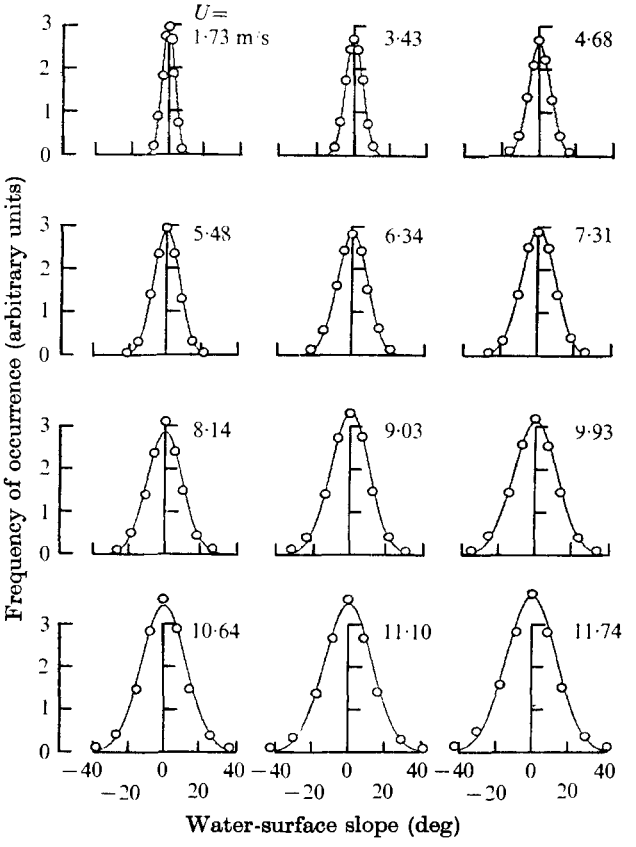

FIGURE 4. Distributions of cross-wind slope under various wind velocities.

various wind velocities are plotted in figure 3, where a negative value indicates a windward slope and a positive value a leeward slope. Distributions of cross-wind slope under various wind velocities are shown in figure 4.

For each wind velocity, the relative frequency of occurrence of various water-surface slopes along both the upwind–downwind and the cross-wind direction was found to follow a normal distribution very closely. The data were first integrated to determine the mean slope, on either side of which the total frequency of occurrence of the water-surface slope is the same. This mean slope is referred to here as the asymmetry of the slope distribution. On the basis of the calculated asymmetry, a Gaussian curve of one of the following forms is fitted to each set of data according to the least-squares principle:

$$f_l = \frac{1}{(2\pi)^{\frac{1}{2}}\bar{\theta}_l}\exp\left(-\frac{(\theta-\theta_{0l})^2}{2\bar{\theta}_l^2}\right) \quad \text{or} \quad f_c = \frac{1}{(2\pi)^{\frac{1}{2}}\bar{\theta}_c}\exp\left(-\frac{(\theta-\theta_{0c})^2}{2\bar{\theta}_c^2}\right), \qquad (1)$$

where the subscripts l and c refer to the upwind–downwind and cross-wind components respectively, f is the frequency of occurrence of a water-surface slope θ, θ_0 is the asymmetry and $\bar{\theta}$ is the variance of the data (centred with respect to θ_0) or the root-mean-square water-surface slope. The fitted curve is drawn as a continuous line for each distribution shown in figures 3 and 4.

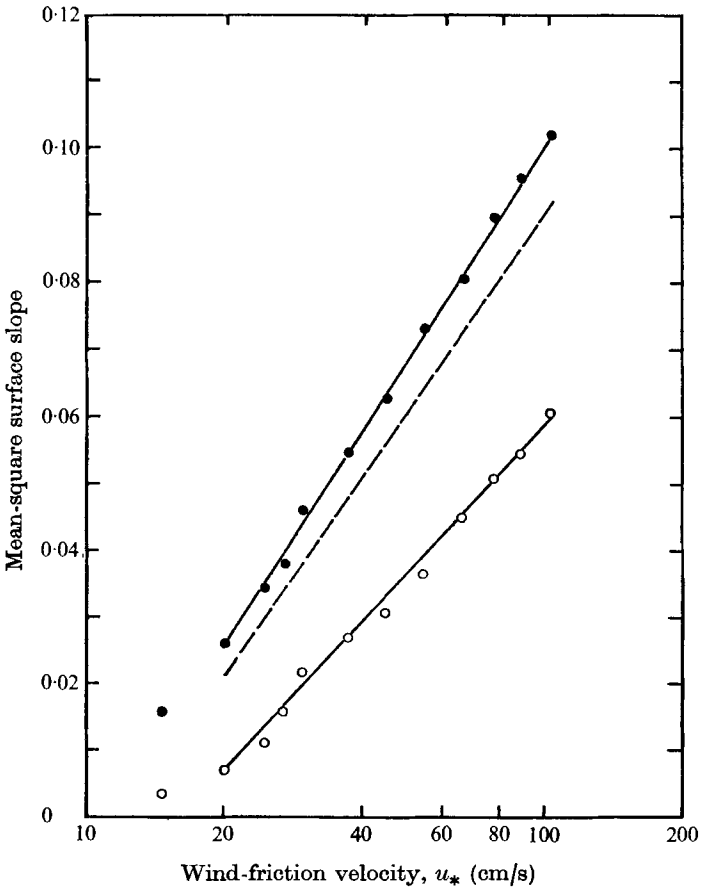

FIGURE 5. Mean-square upwind–downwind and cross-wind slopes under various wind friction velocities. – – –, previous measurements of upwind–downwind slope obtained at a shorter fetch (Wu 1971*a*); ●, upwind–downwind component s_l^2; ○, cross-wind component s_c^2.

The upwind–downwind and cross-wind components of the mean-square surface slope, the square of the variance, are shown in figure 5. Both components of the mean-square surface slope are seen to vary logarithmically with the friction velocity of the wind. Two straight lines have been fitted to the data using the least-squares principle, but excluding the data point at the lowest wind velocity, where the wind boundary layer is not yet turbulent. The mean-square slopes along the upwind–downwind ($\overline{s_l^2}$) and the cross-wind ($\overline{s_c^2}$) directions can be expressed, respectively, as

$$\left.\begin{aligned} \overline{s_l^2} &= 0{\cdot}0466 \ln u_* - 0{\cdot}1139, \quad \overline{s_l^2} = \tan^2\overline{\theta}_l, \\ \overline{s_c^2} &= 0{\cdot}0326 \ln u_* - 0{\cdot}0909, \quad \overline{s_c^2} = \tan^2\overline{\theta}_c, \end{aligned}\right\} \tag{2}$$

where u_* is expressed in cm/s; the error introduced by converting these small angles into slopes as indicated above is negligible. The total mean-square slope $\overline{s^2}$ of the disturbed surface is therefore

$$\overline{s^2} = \overline{s_l^2} + \overline{s_c^2} = 0{\cdot}0792 \ln u_* - 0{\cdot}2048. \tag{3}$$

Besides the friction velocity of the wind, there are other parameters which influence the growth of ripples, and consequently the mean-square slope of the wind-disturbed water surface. These parameters are the surface tension, density and kinematic viscosity of water, and can be combined with the wind friction velocity into a non-dimensional parameter $\rho\nu u_*/T$, where ρ is the density of water, ν is the kinematic viscosity of water and T is the surface tension. Adopting this dimensionless parameter, we can rewrite the above empirical formulae as

$$\left.\begin{aligned}\overline{s_l^2} &= 0{\cdot}0466\ln(\rho\nu u_*/T) + 0{\cdot}2726,\\ \overline{s_c^2} &= 0{\cdot}0326\ln(\rho\nu u_*/T) + 0{\cdot}1795,\\ \overline{s^2} &= 0{\cdot}0792\ln(\rho\nu u_*/T) + 0{\cdot}4521.\end{aligned}\right\} \tag{4}$$

Note that the present experiment was conducted at room temperature (20 °C) with a water temperature of about 16 °C.

Distributions and averages of radius of curvature

A sample distribution of the radius of curvature of the disturbed surface along either the upwind–downwind or the cross-wind direction is shown in figure 2. Because of the limitation on the lower cut-off of detectable curvature of the instrument, a complete distribution of radii of curvature extending to very small radii cannot be obtained. The present measurements, however, are sufficient for determining the average radius of curvature. Any uncertainty at the lower end of the data (the left-hand side of figure 2) would not affect significantly the determination of the centroid of the area under the distribution curve, because the distribution curve always decreases sharply at the lower end.

The average radii of curvature observed for various grazing angles are compiled in figures 6 and 7; the upwind–downwind components are shown in figure 6 and the cross-wind components in figure 7. In both figures, the angular distribution of the average radii of curvature is normalized with respect to their respective frequency of occurrence, or the corresponding slope distribution. This normalization merely involves dividing the observation angle by the variance of the slope distribution. Such a step, relating the average radius of curvature to its relative frequency of occurrence, is helpful for comparing results obtained at various wind velocities with different slope distributions. The relative frequency of occurrence of the radius of curvature required for the converted scale is given, on the basis of the standard deviation, by the Gaussian function shown in (1).

As shown in figure 6, the average radius of curvature in the upwind–downwind direction has its minimum value at a small but positive viewing angle. The average radius generally increases when the observation angle changes continuously from zero to a negative value. For positive viewing angles, the average radius of curvature first decreases to the minimum value, then increases as the observation angle increases. The distribution of the average radius of curvature is generally symmetric in the cross-wind direction, and a larger radius of curvature is obtained at a steeper observation angle.

Each data point in figures 6 and 7 is the average radius of curvature measured for a given viewing angle. The overall average radius of curvature for each wind

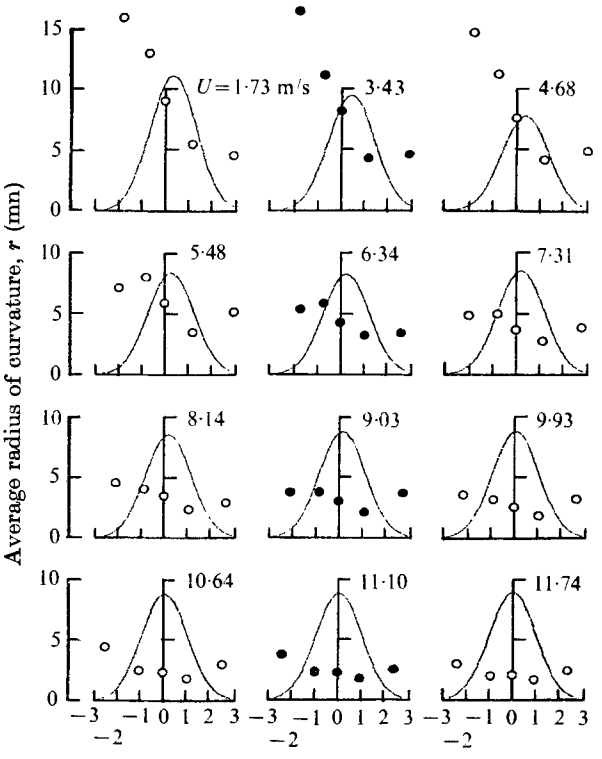

FIGURE 6. Radii of curvature of disturbed water surface obtained for various angles of observation along upwind–downwind direction. The Gaussian curve indicates the frequency of occurrence of the upwind–downwind slope.

velocity can, therefore, be obtained from the grouped data points and their corresponding frequencies of occurrence. The sum of the cross-products of the radii of curvature and their corresponding frequencies of occurrence was first determined, then this sum was divided by the total frequency of occurrence to obtain the overall average radius of curvature of the water surface at a given wind velocity. The results obtained for various wind velocities and along both the upwind–downwind and the cross-wind direction are presented in figure 8.

As the friction velocity of the wind increases, the overall average radius of curvature of the disturbed water surface decreases. There appears to be no systematic deviation between the upwind–downwind and cross-wind components. At high wind friction velocities with the carrier waves covered by ripples, the disturbed surface in the present tank is similar to the air–sea interface. In this case, the overall average radius of curvature is seen in figure 8 to vary as wind friction velocity to the power $-\frac{2}{3}$. The straight line shown in the figure corresponds to

$$\bar{r} = 42 u_*^{-\frac{2}{3}}; \tag{5}$$

in this empirical formula the units for $\bar{r}$ are cm and u_* is again expressed in cm/s. Adopting the non-dimensional parameter used above for the wind friction velocity

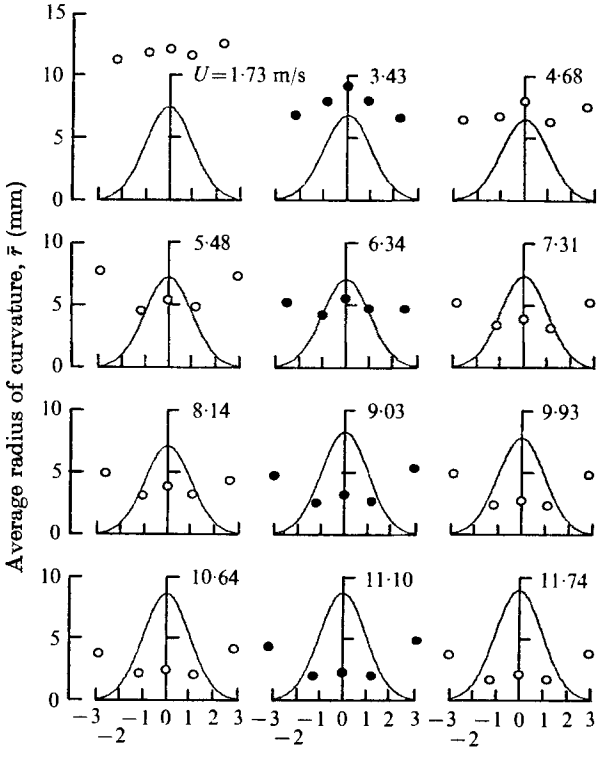

FIGURE 7. Radii of curvature of disturbed water surface obtained for various angles of observation along cross-wind direction. The Gaussian curve indicates the frequency of occurrence of the cross-wind slope.

and the parameters used previously (Wu 1968) to non-dimensionize the roughness length related to capillary waves, we have

$$\rho u_*^2 \bar{r}/T = 3620(\rho\nu u_*/T)^{\frac{1}{2}}. \tag{6}$$

5. Discussion

Symmetry of slope and curvature distributions

The asymmetries of the slope distributions, shown in figures 3 and 4 and discussed earlier, are compiled in figure 9(*a*). For each curvature distribution shown in figures 6 and 7, the first moment of the radius of curvature, with respect to zero slope and weighted according to the frequency of occurrence, was calculated. This moment indicates the asymmetry of the distribution of radius of curvature and is plotted in figure 9(*b*).

The distributions of slope and curvature in the cross-wind direction, shown in figures 4 and 7, are symmetric with respect to zero slope, as no directionality of wave propagation is involved here. The asymmetries of these distributions in the cross-wind direction are seen in figures 9(*a*) and (*b*) to be nearly zero. Both dis-

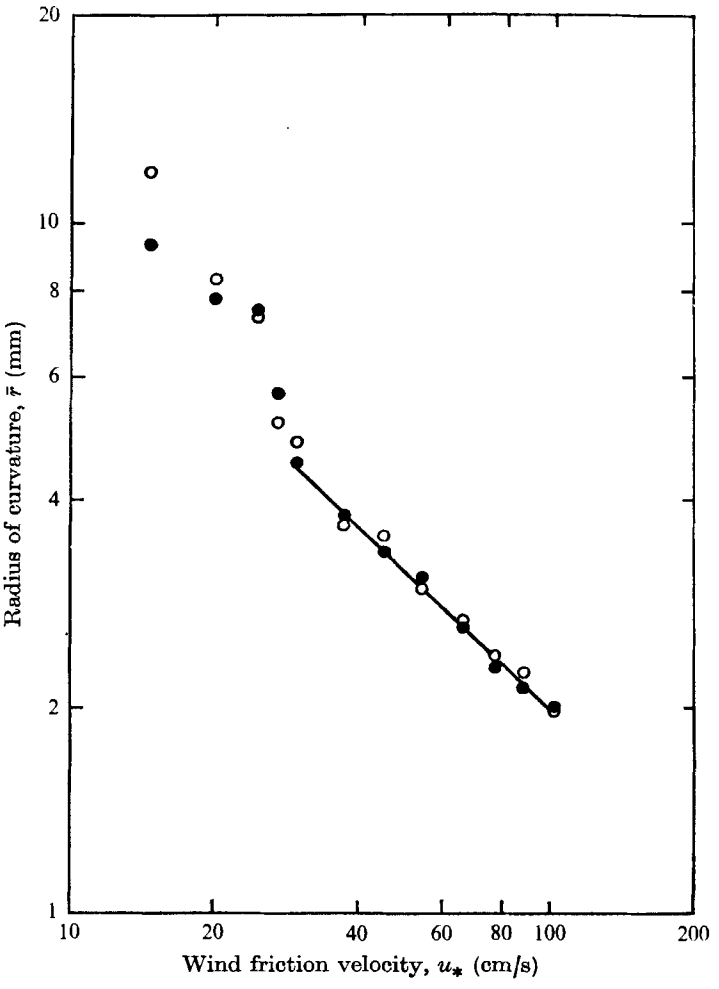

FIGURE 8. Overall average radii of curvature of wind-disturbed surface. ●, upwind–downwind component; ○, cross-wind component.

tributions, however, are asymmetric in the upwind–downwind direction, especially at low wind velocities. Low wind velocities correspond to the regime where surface tension governs wind–wave interaction. As reported earlier (Wu 1971*a*), the asymmetry in this regime is due to the presence of parasitic capillaries on the leeward face of the carrier wave. The slight asymmetry of the slope distribution observed at high wind velocities, corresponding to the gravity-governed regime of wind–wave interaction, is believed to be due to the fact that wave breaking occurs near the crest but on the leeward face of the carrier waves (Wu 1971*b*). Very violent wave breaking was observed near the crest of every dominant wave at the two highest wind velocities. The diminishing asymmetry seen at these two wind velocities in figures 9(*a*) and (*b*) may be due to the fact that some of the three-dimensional roughnesses of the bubbling water surface which accompany breaking waves escape the present optical counting technique but

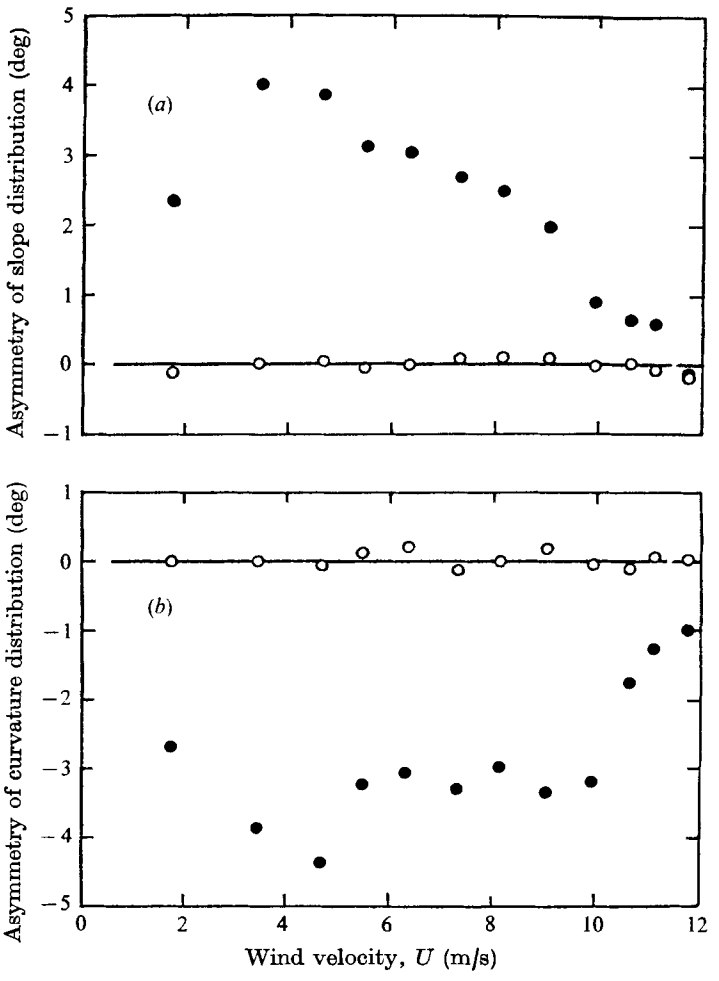

FIGURE 9. Asymmetries of (*a*) slope and (*b*) curvature distributions. ●, upwind–downwind component; ○, cross-wind component.

not the earlier glitter photography (Wu 1971*b*). It is noted that such an asymmetric distribution may cause different back-scattering of electromagnetic waves from the leeward and windward faces of carrier waves respectively.

Isotropy of microstructure of wind-disturbed surface

The ratio of the upwind–downwind and cross-wind components of the mean-square slope is presented in figure 10(*a*). This ratio is seen to increase with the wind velocity first rapidly and then gradually. At very low wind velocities, the parasitic capillaries are the major contributors to the mean-square slope. These capillaries are long crested in comparison with their wavelength, and generally propagate along the wind direction; therefore in this case the cross-wind slope is very small. As the wind velocity increases, resonant waves are produced. These resonant waves, the longer of which carry parasitic capillaries, generally propa-

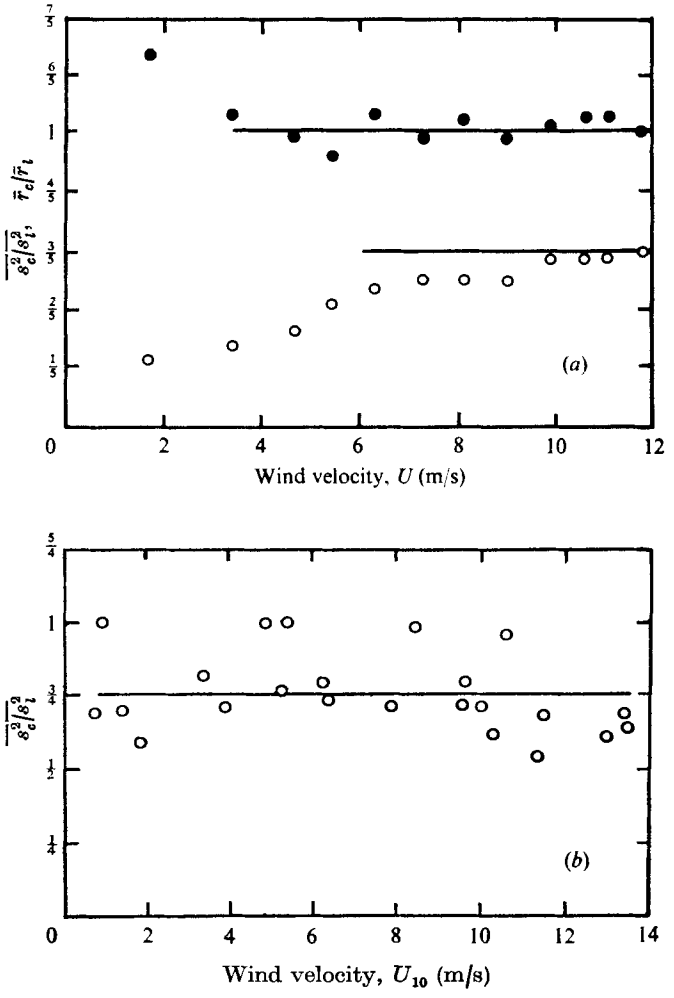

FIGURE 10. Isotropy of microstructure of wind-disturbed surface. (*a*) Laboratory results: ratio of cross-wind and upwind–downwind components of mean-square slope (open circles) and average radius of curvature (solid circles). (*b*) Oceanic results: ratio of cross-wind and upwind–downwind mean-square slopes.

gate at large angles from the wind direction. Consequently, the cross-wind slope becomes relatively more important. At high wind velocities in the gravity-governed regime of wind–wave interaction, the carrier waves are almost unidirectional, but their profiles are well covered by random short waves. In this case, the ratio of the cross-wind and upwind–downwind slopes varies only slightly with the wind velocity and is seen in figure 10(*a*) to approach asymptotically a value as high as $\frac{3}{5}$.

The ratio between the cross-wind and the upwind–downwind components of the overall average radius of curvature is also shown in figure 10(*a*). Although there is some scatter in the data, it is clear that this ratio has a value close to one for all wind velocities in both regimes of wind–wave interaction.

The carrier waves in the present tank are definitely directional, propagating predominantly along the direction of the wind. The carrier waves described by the wave-height statistics, however, have only secondary effects on the root-mean-square slope of the disturbed surface. This slope is the statistical average of the first derivative of wave height, and is dominated by the ripples. Consequently, despite the fact that the carrier waves are essentially unidirectional at high wind velocities, the slope statistics are much more isotropic than the height statistics. The statistics of surface curvature are seen in figure 10(*a*) to be isotropic, because the curvature statistics (the second derivative of wave height) are dominated by the smallest waves. In summary, the present results indicate that the *microscopic* structure of wind waves is isotropic, and that the wave structure is less isotropic for longer wave components. The wavenumber ranges of isotropy for various structures, however, cannot be deduced from the present data, which were not spectrally resolved.

Cox & Munk (1956) deduced slopes of the sea surface from the brightness distribution in photographs of sun glitter on the sea surface. The ratio of the cross-wind and upwind–downwind components of the mean-square sea-surface slope is plotted in figure 10(*b*), where U_{10} is the wind velocity measured 10 m above the mean sea level (Wu 1972*b*). From comparison with figure 10(*a*), these ratios obtained from oceanic data are similar to those determined from laboratory results obtained at high wind velocities in the gravity-governed regime of wind–wave interaction. This is understandable, as the surface-tension-governed regime existing in laboratory tanks at low wind velocities never exists in the field (Wu 1972*c*). Wind–wave interactions on oceanic scales fall into the gravity-governed regime for all wind velocities. The overall average ratio of the two components of the mean-square sea-surface slopes is seen in figure 10 (*b*) to be about $\frac{3}{4}$, indicating only an approximate isotropic spreading of high frequency waves. Limited by the width of the tank, the value of the same ratio measured in the laboratory is only about $\frac{2}{5}$. However, the difference may be small enough to permit reasonably accurate modelling of the microstructure of the sea surface in a laboratory wind-wave tank.

Saturation of high frequency waves

The mean-square surface slopes measured at two different fetches in the present tank are compared in figure 5. The values obtained earlier at a shorter fetch (7 m) are seen to be smaller than those obtained here at a longer fetch (11 m). The mean-square slope of the wind-disturbed water surface can be obtained from the directional wavenumber spectrum $\Psi(\mathbf{k})$, or

$$\overline{s^2} = \int_{k_0}^{k_\nu} k^2 \Psi(\mathbf{k})\, d\mathbf{k}, \tag{7}$$

where k and $\mathbf{k}$ are the scalar and vector wavenumber respectively, k_0 is the wavenumber at the spectral maximum and k_ν is the neutrally stable wavenumber. The latter corresponds to the wavelength at which the energy input from the wind is balanced by the energy dissipation through viscosity. The

contribution from the wavenumber range $k < k_0$ to the mean-square slope is negligible, while the neutrally stable wavenumber serves as the upper cut-off.

The increase in the mean-square slope observed in figure 5 for the case of longer fetch cannot be accounted for by extension of the equilibrium wave spectrum at either the low or high frequency end. Undoubtedly the carrier waves grow with the fetch; however, their contribution to the mean-square surface slope as a result of a slight decrease in k_0 is negligible. The equilibrium portion of the spectrum at the longer fetch cannot be expanded to higher frequencies than that at the shorter fetch, because the friction velocity of the wind at the longer fetch is slightly smaller than that at the shorter fetch (Wu 1968, 1975). Altogether, the present results appear to indicate an overall increase in energy density over the entire spectrum at a longer fetch. In other words, even the high frequency portion of the wave spectrum is saturated locally, but the spectrum is not universal. The present data, however, are too limited to indicate this variation quantitatively.

Comparison between laboratory and field results

Because of the great difference between the wind fetches in the wind-wave tank and in the field, the friction velocity rather than the wind velocity is used here as the basis for comparison of slope data. Adopting a logarithmic wind profile, the friction velocity for Cox & Munk's data can be calculated from either their own velocity measurements at two different heights (12·5 and 2·75 m above the mean sea level) or from the wind velocity measured at 12·5 m and the approximate formula for the wind stress coefficient C_{10}: $C_{10} = 0{\cdot}5U_{10}^{\frac{1}{2}} \times 10^{-3}$. The friction velocities calculated by means of the two methods are about the same, but the results obtained with the latter method are used because the wind velocity measured at the lower height (2·75 m) may be too close to the water surface to be free from wave-induced motion, especially at high wind velocities. The present results and the field data are plotted versus the friction velocity of the wind in figure 11.

The directional wave spectrum in the equilibrium range was proposed by Phillips (1966, chap. 4) as

$$\Psi(\mathbf{k}) = \begin{cases} B\pi^{-1}k^{-4} & \text{(gravity range)}, \\ B'\pi^{-1}k^{-4} & \text{(capillary range)}, \end{cases} \tag{8}$$

where B and B' are the spectral coefficients for the gravity and the capillary ranges respectively. These coefficients were originally considered to be constant but have recently been recognized as fetch dependent. Substituting (8) into (7), we have

$$\overline{s^2} = B \ln (k_\gamma/k_0) + B' \ln (k_\nu/k_\gamma), \tag{9}$$

where k_γ is the wavenumber at which the influence of surface tension on wave propagation becomes negligible. It has been shown (Wu 1972*b*) that oceanic slope data (Cox & Munk 1956) may be divided into two groups. Gravity waves are the sole contributors to sea-surface slope at low wind velocities, with the right-hand side of (9) consisting only of the first term; both gravity and capillary waves contribute to sea-surface slope at high wind velocities, with the right-hand

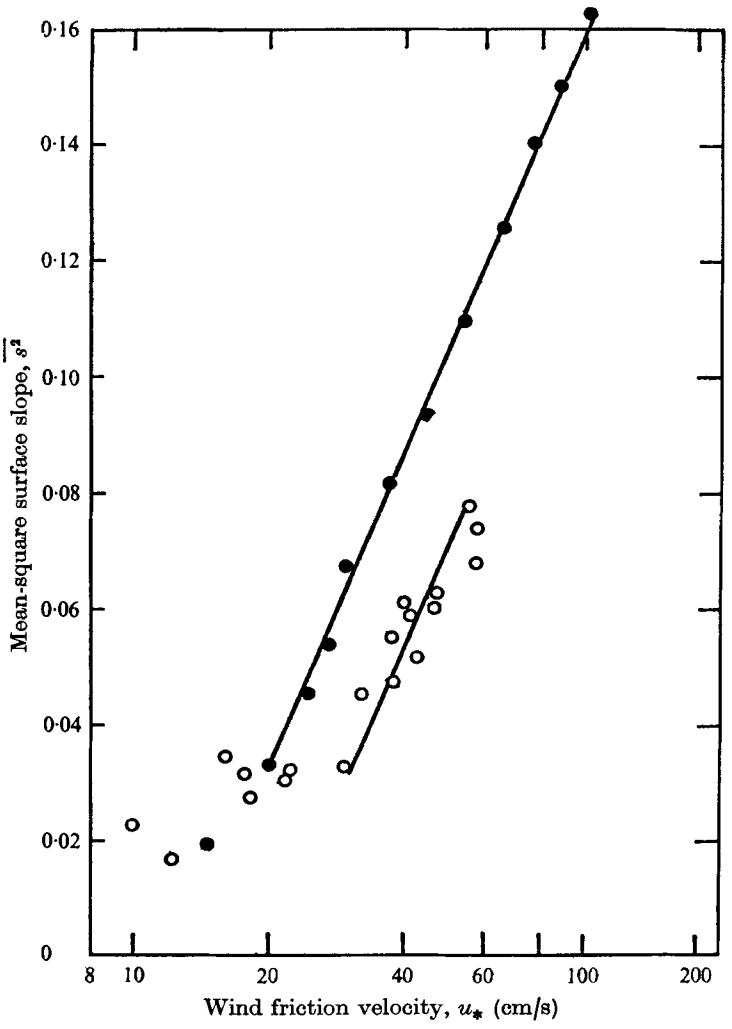

FIGURE 11. Comparison of laboratory and field results for mean-square surface slope. ●, present results; ○, field results (Cox & Munk 1956).

side of (9) consisting of both terms. The portion of the oceanic data fitted by a straight line in figure 11 is the second group. A straight line is also drawn to fit the laboratory data in figure 11. It is interesting to see that the fitted line for the laboratory data with contributions from both gravity and capillary waves is parallel to the line fitted through the oceanic data with the same contributors. This fact appears to indicate that the spectral coefficients B and B' have a much larger value in the laboratory tank than in the field.

This result that the mean-square slopes measured in the laboratory with short dominant waves are much larger than those measured in the field with long dominant waves is consistent with our earlier findings (Wu 1973). With pre-existing long surface waves, the mean-square slope under identical wind friction velocity was found to be smaller than without pre-existing long surface waves.

The explanation for this is that the long waves, acting like an energy sink, prevent the growth of waves of intermediate lengths, which contribute much more heavily to the mean-square slope than the longer components. These results are consistent with those of Phillips & Banner (1974), who showed analytically that long waves suppress the growth of short waves when the latter are at the point of incipient breaking.

6. Conclusions

The present results provide the first systematic statistical description of the microstructure of a wind-disturbed water surface. The slope distributions of the surface are closely Gaussian along both the upwind–downwind and the cross-wind direction. Both slope components are found to vary logarithmically with the friction velocity of the wind. Despite the narrowness of the tank, the ratio of the cross-wind and upwind–downwind mean-square slopes becomes as high as $\frac{3}{5}$ in the gravity-governed regime of wind–wave interaction. The ratio of the cross-wind and upwind–downwind components of the average radius of curvature is close to one at all wind velocities. The results indicate that the microstructure of the surface is always nearly isotropic, and that the structure of longer wave components is less isotropic. The mean-square slope measured at a shorter fetch is greater than that obtained at a longer fetch, suggesting that even the high frequency portion of the wave spectrum is saturated locally, but that the saturated state changes with fetch. The laboratory-determined mean-square slope is found to be much larger than the oceanic value. This is believed to be due to the long waves absorbing most of the energy supplied by the wind and preventing the growth of intermediate components.

The experimental part of this work was done at Hydronautics, Incorporated. I am grateful for the earlier support of the Advanced Research Project Agency and to the present sponsor, Fluid Dynamics Program, Office of Naval Research under Contract N00014-75-C-0285.

REFERENCES

Cox, C. S. 1958 Measurements of slopes of high-frequency wind waves. *J. Mar. Res.* **16,** 199–225.

Cox, C. S. & Munk, W. H. 1956 Slopes of the sea surface deduced from photographs of sun glitter. *Scripps Inst. Oceanog. Rep.* vol. 6, no. 9.

McGrath, J. R. & Osborne, M. F. M. 1973 Some problems associated with wind drag and infrared images at sea surface. *J. Phys. Oceanog.* **3,** 318–327.

Newton, R. W. & Rouse, J. W. 1972 Experimental measurements of 2·25 cm backscatter from sea surfaces. *I.E.E.E. Trans.* no. GE-10, pp. 2–7.

Phillips, O. M. 1966 *The Dynamics of the Upper Ocean.* Cambridge University Press.

Phillips, O. M. & Banner, M. L. 1974 Wave breaking in the presence of wind drift and swell. *J. Fluid Mech.* **66,** 625–640.

Schooley, A. H. 1954 A simple optical method for measuring the statistical distribution of water surface slopes. *J. Opt. Soc. Am.* **44,** 37–40.

Wu, J. 1968 Laboratory studies of wind–wave interactions. *J. Fluid Mech.* **34,** 91–112.

Wu, J. 1971*a* Slope and curvature distributions of wind-disturbed water surface. *J. Opt. Soc. Am.* **61**, 852–858.

Wu, J. 1971*b* Observations on long waves sweeping through short waves. *Tellus*, **23**, 364–370.

Wu. J. 1972*a* Surface curvature of wind waves observed from different angles. *J. Opt. Soc. Am.* **62**, 395–400.

Wu, J. 1972*b* Sea-surface slope and equilibrium wind-wave spectra. *Phys. Fluids*, **15**, 741–747.

Wu, J. 1972*c* Physical and dynamical scales for generation of wind waves. *J. Waterways Harbors Coastal Engng Div. A.S.C.E.* **98** (WW2), 163–175.

Wu, J. 1973 Correlation of micro- and macroscopic structures of wind waves and differential roughening and smoothing of surface waves by wind. *Hydronautics. Inc. Tech. Rep.* no. 7211–6.

Wu, J. 1975 Wind-induced drift currents. *J. Fluid Mech.* **68**, 49–70.

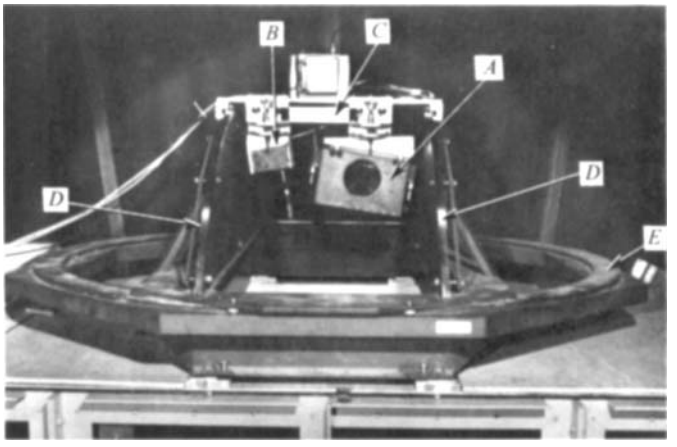

(*a*)

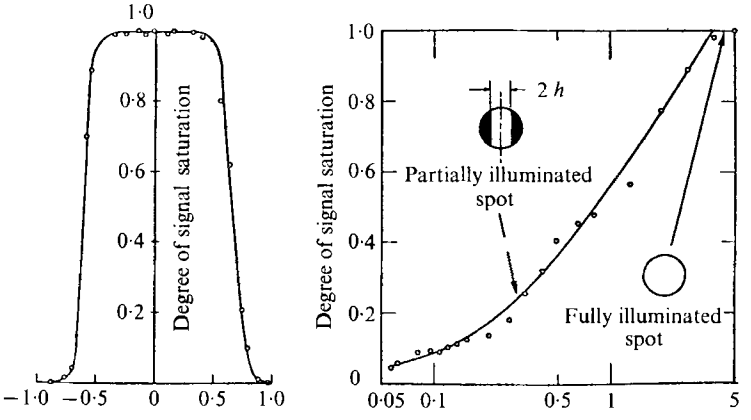

(*b*) (*c*)

FIGURE 1. (*a*) Optical instrument: *A*, light source; *B*, light receiver; *C*, carriage; *D*, vertical arc; *E*, base ring. (*b*) Slope and (*c*) curvature responses of optical instrument.

(*Facing p.* 480)